GEOTECHNICAL CHARACTERISATION OF THE MIOCENE FORMATIONS AT THE LOCATION OF IVENS SHAFT, LISBON

António Pedro[1*], Lidija Zdravković[2], David Potts[2] & Jorge Almeida e Sousa[1]

[1]Department of Civil Engineering, *University of Coimbra, Coimbra, Portugal*

[2]Department of Civil and Environmental Engineering, *Imperial College, London, UK*

*Corresponding author (e-mail: amgpedro@dec.uc.pt)

ABSTRACT

The design of complex underground structures in an urban environment requires in the first instance an appropriate characterisation and interpretation of the ground conditions and of the mechanical behaviour of soil formations in the ground profile. With such information it is then possible to select and calibrate appropriate soil constitutive models for application in advanced numerical analysis, with the objective of predicting the induced ground movements and the potential damage to existing structures and services. This paper provides an interpretation of the site investigation data collected for the numerical analysis and design of the Ivens shaft excavation in Lisbon, Portugal. For the first time a comprehensive set of interpreted data is obtained for two of the main formations in the Lisbon area, *Argilas e Calcários dos Prazeres* (AP) and *Areolas da Estefânia* (AE), improving the understanding of their mechanical behaviour and making the data available for application in most soil constitutive frameworks. It is evident from the results that even with careful testing procedures the data may appear to be inconsistent, requiring further assumptions when deriving soil parameters. Such assumptions are discussed and an emphasis is placed on the need to combine data from laboratory and field investigations.

1 INTRODUCTION

The Baixa-Chiado metro station is one of the most important interface stations of the Lisbon Metro network, as it enables the interchange between the busy Green and Blue lines and is located near downtown Lisbon (Figure 1). Apart from the two galleries that accommodate the platforms, the Baixa-Chiado station also has two exit tunnels, Chiado and Crucifixo (Postiglione et al., 1997). A third exit via a 40m deep shaft is also included in the original project but its construction has been successively delayed to date (late 2017). Due to space constraints the shaft was positioned in the backyard of the Quintão building, with access via the Ivens street, and is surrounded by old buildings and services (hatched areas in Figure 1). The shaft, named Ivens, is of a complex shape, varying from an elliptical cross section at the ground surface to a circular cross section at its base.

Several previous ground investigation reports were available for the design of the Ivens shaft, relating to various locations in Lisbon (Moitinho de Almeida, 1991; Marques, 1998; Cenorgeo, 2008; Guedes de Melo, 2008). These have established the ground profile and enabled some characterisation, mainly through field testing, of the two main formations, geologically referred to as Miocene: the predominantly silty-clayey *"Argilas e Calcários dos Prazeres"* or the *AP* formation; and the predominantly granular "Areolas da Estefânia" or the *AE* formation. Limited laboratory testing existed, in particular the assessment of the soils' nonlinear small strain stiffness behaviour.

A ground investigation conducted in 2010 reported by Pedro (2013) was aimed at providing more reliable geotechnical data for the numerical analysis of ground movements caused by shaft excavation. A particular effort was directed to the interpretation of the small strain stiffness, as this aspect of soil behaviour is most influential in predicting ground movements (e.g. Addenbrooke et al., 1997; Franzius et al., 2005; Zdravkovic et al., 2005). The paper brings together the existing and new site investigation data and interprets the main mechanical parameters of strength, stiffness and compressibility of both formations.

INSERT FIGURE 1 HERE

2 GEOLOGICAL PROFILE AT THE IVENS SHAFT SITE

The geology of Lisbon has been influenced by several extreme geological processes (Antunes, 1979; Alves et al., 1980). The oldest superficial soils date from the Cretaceous period, 95 million years ago (Ma), although the majority of the city centre is founded upon Miocene formations, formed around 24Ma ago (Moitinho de Almeida, 1991). During this epoch several transgressive-regressive cycles, each corresponding to a depositional sequence, occurred due to tectonic events and due to variations in sea level (Dias & Pais, 2009). This epoch was followed by the last glacial period, when a substantial climate change in the region caused intense erosion and a deflection in the course of the river Tagus (Dias et al., 1997). Only at the beginning of the current Holocene epoch did the water level start to rise again and new sediments began to deposit in the basin.

The lithological profile at the Ivens shaft site is shown in Figure 2. The top 6 m is a loose sandy fill. Underneath are the two main formations, *AE* down to 35 m, followed by the AP formation. The *AP* formation was deposited in a marine environment which changed progressively to a sub-tidal zone in shallower waters. The material between 35 and 37 m depth can be considered a different unit (Top *AP*), as it is lighter in colour (more oxygen) and is more compatible with the latter type of environment. The analysis of the *AE* formation is more complicated since it contains layers of different degrees of cementation, as a result of significant differences in the depositional environment (Cotter, 1956; Antunes et al., 2000). At depths between 12 and 17 m within the AE formation there is a 5 m thick layer of fossiliferous limestone, which is usually formed in shallow, quiet and warm waters, the conditions often associated with tidal flats or reef environments. Despite significant variations within the *AE* formation, it is usually considered in the literature as a single unit, with the exception of the limestone layer which is considered independently. The water table was measured at approximately 27 m depth.

The particle size distribution (PSD) determined by Pedro (2013) at each metre depth, with the exception of the limestone layer, is presented in Figure 3. The PSDs for the AP formation (below 35 m depth) are almost identical, with around 23 % of clay, 62 % of silt and only 15 % of mostly fine sand. In contrast, the results of the AE formation indicate differences which can be related to depth and to past geological events. The layer above the limestone, between 5 and 12 m, is a finer soil since it comprises nearly 44 % of silt and 14 % of clay on average, while the lower layer (18 to 34 m) consists of an average of 80 % of sand (mostly fine) and 16 % of silt. According to the ASTM (2006) standard the AP formation is classified as a lean clay (CL), while the AE formation, despite its variability throughout the profile, can be classified as a silty sand (SM). The fill is fairly homogeneous with 93 % of fine sand and is classified as a poorly graded sand (SP).

3 NEW GEOTECHNICAL INVESTIGATION

The new ground investigation involved drilling of two new boreholes (B1 and B2) in the backyard of the Quintão building (Figure 1) to about 40 m depth. Figure 2 shows positions in the ground profile from which 76 mm diameter samples were taken. The boreholes were primarily drilled using rotary techniques to provide cores of 76mm diameter to enable almost continuous sampling of the soil. However, at specific depths, where good quality samples were required, instead of coring a thin-walled sampler with a PVC liner of also 76mm diameter was used. After the extraction, the coring resumed until another specific extraction depth was reached. High recovery rates were obtained in the finer materials while in the coarser materials, particularly those located below the water table (27m depth), only partial recovery was achieved. Apart from retrieving samples, *disturbed* for identification of the lithology and determination of the physical properties, and *intact* for advanced laboratory testing, the investigation also included seismic tests for characterising the initial stiffness of the soils. Unfortunately, due to obstructions met in both boreholes it was only possible to perform down-hole tests to a depth of 28 m.

Due to the granular nature of the *AE* formation the sampling of intact samples was not straightforward, which is why prior investigations of the strength and stiffness of this material mainly relied on indirect correlations with in-situ tests, such as the Ménard Pressuremeter Test, MPT (Guedes de Melo, 2008) or Self-Boring Pressuremeter Test, SBPT (Ludovico Marques & Sousa Coutinho, 2004). However, in the new investigation it was possible to retrieve intact samples from this formation using the methodology mentioned (Pedro, 2013). As soon as the samples were retrieved, and while laterally confined by the PVC tube, they were fully wrapped in wax in order to preserve their natural properties and minimise any disturbance. All samples were then placed into a moisture controlled chamber until preparation and testing in a temperature controlled laboratory.

A total of 34 tests were conducted by Pedro (2013) in the Geotechnical laboratory of Coimbra University in Portugal. A summary of all tests and their initial conditions are presented in Table 1 in the Appendix. The experimental programme comprised three oedometer and four isotropic triaxial compression tests, for assessing the behaviour in compression, six isotropic triaxial compression tests with bender element measurements for analysing the initial stiffness, and 21 triaxial tests for evaluating the strength and deformation of the soils in the two formations. The oedometer samples were 50 mm in diameter and 19 mm thick. The triaxial samples were 38 mm in diameter and 76 mm high. All samples were initially saturated to a minimum B-value of 0.95 (up to 0.98 in the case of the AE samples).

In the AE formation a total of 14 samples were isotropically consolidated in a triaxial apparatus to different levels of the mean total stress, p_i, 9 of which then followed compression and 5 extension stress paths. These tests were divided into 3 main groups, each with a purpose of investigating a specific aspect of soil behaviour. In order to evaluate the small strain stiffness behaviour independently of the p'-effect, 6 tests, 3 in compression (PC) and 3 in extension (PE), were performed with constant p'. A second group of tests were sheared following total stress paths expected to apply to the shortest and longest axes of the elliptical shaft during excavation, as sketched in Figure 4 for the shaft's horizontal cross-section. With the vertical total stress being approximately constant in the soil around the shaft at any horizontal section, a triaxial compression path with decreasing p (CD), due to a decreasing total horizontal stress, is expected in the short axis of the shaft. Conversely, a triaxial extension path with increasing p (EI) is expected in the long axis, due to an increase in the horizontal total stress. An additional test in extension with a decreasing p (ED) was also performed in order to simulate the total stress path followed by a soil element located above the enlargement of the shaft section, as shown in Figure 4 for the shaft's vertical cross-section. In this case the vertical stress reduces due to the shaft excavation beneath. Finally, a third group of compression tests follows a conventional compression stress path with an increasing p (CI), in order to facilitate the understanding and interpretation of all results and enable a comparison with other soils. Since the majority of the samples were collected at 3 different depths (8, 18 and 21 m), the tests were performed at approximately those three in-situ stress conditions, represented by p’ of 130, 300 and 400 kPa, respectively. The 7 samples tested in the AP formation (2 from the Top AP unit) were all collected from between 36.3 and 40.4 m depth and consequently the estimated vertical field stress varied from 585 to 630 kPa. Due to limitations of the maximum working pressure of the triaxial cell all tests were performed with an initial p’ of 480 kPa. However, in order to compare the effects of the initial stress state 2 samples had an initial isotropic stress state while the remainder were consolidated under anisotropic conditions (K_0=0.7). A similar strategy was adopted for this formation regarding the shearing stress paths. However, in this case and given the limited number of samples available, not all the different stress paths could be tested as for the AE formation.

INSERT FIGURE 2 HERE

INSERT FIGURE 3 HERE

INSERT FIGURE 4 HERE

4 IN SITU STRESSES

The new ground investigation at the Ivens shaft site did not include tests to estimate the in-situ stress profile. However, results from several SBPTs conducted by the National Laboratory for Civil Engineering (LNEC, 1996a, b, c, d) were available from previous investigations and were recalculated by the authors taking into consideration the water table position measured at the Ivens site by Pedro (2013). This enabled a more accurate estimation of the coefficient of earth pressure at rest, K_0 (Figure 5), albeit with some scatter. Despite this it is possible to establish that the K_0 value in the *AE* formation appears to decrease with increasing vertical effective stress from a maximum of about 1.5 at 200 kPa to approximately 0.7 at 500 kPa. The results obtained for the *AP* formation show a smaller variation of K_0, with average of 0.7. The high K_0 values in the top part of the AE formation are thought to be consistent with the geological history discussed earlier, and in particular glaciation and erosion of the deposits.

INSERT FIGURE 5 HERE

5 PHYSICAL PROPERTIES

X-Ray diffraction tests on samples collected in the new ground investigation revealed that quartz is the predominant mineral in both formations (60%), followed by feldspar (15%). The *AP* formation also contains reasonable amounts of mica-illite (11%) and smectite (9%) which may affect the compressibility characteristics of the soil if variations in the water content occur (Skempton, 1953). The intact samples collected at different depths enabled the definition of profiles of plasticity index, activity, unit weight, moisture content, void ratio and degree of saturation, as presented in Figure 3. Despite some scatter, typical of natural soils that exhibit variability due to different depositional environments, it is interesting that these properties seem broadly constant with depth, independent of the lithology. Both formations have a unit weight of approximately 20 kN/m^3, a water content of around 20 %, and a void ratio below 0.7. Apart from the coarser zones below the Limestone layer, the soil appears to be saturated. The Atterberg limits of the *AP* formation suggest that the formation should have low compressibility, since the water content of soil is at or slightly below the plastic limit (about 25 %) and the liquid limit increases with depth from 40 % at 36m depth to about 50% at 40m depth. Despite the low plasticity index in Figure 3, the activity can be considered medium to high according to Skempton (1953). These values support the conclusions of the mineralogical analysis that the clay fraction is sensitive to variations in the water content.

6 BEHAVIOUR IN COMPRESSION

Figure 6 shows the results of 4 isotropic compression tests (denoted 'I') on intact samples collected from two boreholes at the Ivens shaft site (Pedro, 2013). Two of the samples, I-*AE*-08.5 and I-*AE*-21.5, taken from 8.5 and 21.5 m depth respectively, show almost identical behaviour in compression, with the interpreted gradient of the normal compression line (NCL) being λ=0.134. The volumetric strain measured in test I-*AE*-18.0, for a similar change in p', is significantly lower, with interpreted λ=0.089. This sample was collected from 18 m depth, immediately below the limestone, and is therefore likely to have some cementation which contributes to its low compressibility. Consequently, a representative NCL for the *AE* formation is taken as that with λ=0.134. In contrast, the swelling paths, both from the unload-reload loops and from the final unloading, are similar for all AE tests, and a representative gradient is κ=0.033.

A single isotropic compression test on the *AP* formation indicates a compression gradient λ=0.178, and a swelling gradient κ=0.066. The gradients for both formations are within the expected range of values found in the literature for materials with similar gradings (Atkinson, 1993). To assess the existence of structure in the *AP* soil, additional oedometer tests were performed on intact samples of 'fair' quality, according to the approach proposed by Lunne et al. (1997). The results are compared in Figure 7 with the intrinsic compression line (ICL) determined using Equations 1 and 2 proposed by Burland (1990).

$$C_C^* = 0.256 \cdot e_L - 0.04 \quad (1)$$

$$e_{100}^* = 0.109 + 0.679 \cdot e_L - 0.089 \cdot e_L^2 + 0.016 \cdot e_L^3 \quad (2)$$

Where C_C^* represents the intrinsic compression index, e_{100}^* the void ratio at a vertical effective stress of 100 kPa and e_L the void ratio at liquid limit (taken as 1.096). The responses of the two deeper samples (O-AP-37.5 and 40.0) plot above the ICL and yield at higher stresses, confirming the existence of structure. The degradation of structure with further compression is not rapid and an average sensitivity of the clay (Cotecchia & Chandler, 2000), of about 3 was determined. In contrast, the shallower sample O-AP-36.5 appears to follow the intrinsic compression line, behaving more like a reconstituted material. These results are in agreement with the proposed geological framework in Figure 2, in that the top of the *AP* formation is a separate less-structured layer, while the rest of the formation is clearly structured. The results from the 3 tests show that the *AP* formation is over-consolidated, with the OCR, determined using Taylor (1948) method, varying from 3.4 to 5.6.

Furthermore, oedometer results show no significant creep displacements and enable an estimation of a coefficient of permeability of about $2 \cdot 10^{-10}$ m/s to be made for the in-situ stress level.

INSERT FIGURE 6 HERE

INSERT FIGURE 7 HERE

7 DRAINED STRENGTH PARAMETERS

7.1 AE FORMATION

Figures 8 to 11 show the shearing behaviour of all *AE* samples under both drained and undrained conditions. The applied shearing rate was 5% of axial strain per day, which was sufficient to ensure no excess pore pressures in the former and uniform excess pore pressures in the samples in the latter type of shearing (both checked with a mid-height pore pressure probe). Generally, the soil displays dilatant behaviour in both compression and extension, with most samples showing post-peak strain-softening in Figure 8, with the peak strength occurring at axial strains between 2 and 6 %. Shearing to about 20% axial strain, ε_a, has not established clear critical state stress ratios, q/p', in either of the two shearing modes. In terms of the volumetric response, the samples tested under drained conditions exhibited an initial contraction followed by dilation (Figure 9). Tests in extension with a constant p' (*T-AE-DPE-I*) show a consistent effect of the mean effective stress level p_i', with a sample sheared from 400 kPa exhibiting the smallest dilation, while that at 130 kPa the largest. Similarly, the tests in compression at constant p' (*T-AE-DPC-I*) also reveal higher dilation at lower stress levels, although the test at $p' = 130$ kPa has stopped prematurely. In general samples sheared in compression show higher volumetric dilation than those sheared in extension. However, despite the measured final volumetric strains differing significantly, the initial gradients of dilation $(|\Delta\varepsilon_a|/\Delta\varepsilon_v)$ appear to be similar for these samples, as shown in the figure. The two additional standard drained tests in compression (*T-AE-DCI-I*) presented higher contractive volumetric strains followed by dilation, with this behaviour being more evident in the case of the smaller p'. The excess pore water pressures in the undrained tests (Figure 10) varied from sample to sample, in conjunction with the applied modes of shearing explained earlier in Figure 4, but their overall trend was again negative at high strains. These interpretations confirm the behaviour of the *AE* formation to be characteristic of dense granular soils with most of the observed differences being a result of the natural variability of the formation, as ascertained from Figure 3, and particularly of the stress conditions and paths imposed during shearing.

As noted above, no clear ultimate strength conditions could be identified from all samples, particularly those tested in extension. However, the analysis of the effective stress paths from all 14 tests is helpful in interpreting the likely peak strength envelopes in compression and extension (Figure 11). Marked on the figure are also the points of the maximum stress ratio (q/p’) for all stress paths. Despite the scatter observed in the results and the variability in this formation (Figure 3) the strength envelopes determined present a very good fit, indicating an angle of shearing resistance of 42°, in both compression and extension, with no apparent cohesion. Furthermore, despite failing to reach convincing critical state conditions, an angle of shearing resistance of about 35° was determined from the stress ratio q/p’ achieved at highest strain levels.

INSERT FIGURE 8 HERE

INSERT FIGURE 9 HERE

INSERT FIGURE 10 HERE

INSERT FIGURE 11 HERE

7.2 AP FORMATION

Seven triaxial compression tests were performed on intact samples from the AP formation, the results from which are presented in Figures 12 to 15. The same shearing rate of 5%/day was applied, but in this case both from isotropic and K_o initial stresses. Although all samples are taken from practically the same depth of the deposit, the striking feature from the figures is a large variation in the observed responses. However, the response from all samples is consistent with the behaviour of overconsolidated clays. Some of the differences in the results are also related to the different stress and shearing conditions imposed in the tests and to the inherent variability of the deposit. The shearing behaviour presented in Figure 12 exhibits varying degrees of strain-softening, consistent with a break-down of structure. The evolution of the volumetric strains in Figure 13 from the 4 drained tests is highly variable, but all samples show dilation towards final states. The effect of the initial stress state for the same initial p' is evident from samples *T-AP-DPC-K* and *T-AP-DPC-I*, with the latter showing higher contractive volumetric strains as it starts shearing further from the strength envelope. A similar level of variability is observed in the pore pressure response measured in the 3 undrained tests, but the overall tendency is one of generating negative excess pore pressures towards failure (Figure 14). Also the tests performed with an increase in p' (UCI) generated initially positive excess pore pressure while that with a decrease in p' (UCD) generated negative excess pore pressure from the start of shearing.

The behaviour exhibited by the two samples retrieved from 36.3 and 37.7 m depth in the TAP layer, T-*TAP*-DPC-I-480 and T-*TAP*-UCI-K-480, differs from that observed in other samples, despite having similar mineralogical and PSD curves. Both samples show a mild strain-softening (Figure 12), absence of bonding, a more pronounced contraction (Figure 13) and a high positive excess pore water pressure (Figure 14) generated at the beginning of shearing, typical of reconstituted samples. When plotting the effective stress paths of these tests in Figure 15 the points of their maximum stress ratio are not aligned with the remaining points, making it difficult to establish a unique peak strength envelope for the *AP* formation. When considering all tests, a ϕ' and an apparent c' of 31° and 162 kPa can be estimated, respectively, although with low confidence (low R^2). Much better agreement is obtained when the two TAP samples are not considered, with values of ϕ' and c' being estimated to be 45° and 103 kPa, respectively. These discrepancies are again in agreement with the proposed geological framework presented in Figure 2, with samples deeper than 38 m indicating considerable bonding and high c’ (the samples would not disintegrate if submerged in water), while others, between 35 and 38 m depth, exhibiting minimal or even non-existent structure. Similar difficulties were observed for the evaluation of the critical state angle of shearing resistance in this formation. A value of 28° was estimated when neglecting the results of the TAP samples. These shearing results further confirm that the top of the AP layer (TAP) should be considered as a different unit in the ground profile.

INSERT FIGURE 12 HERE

INSERT FIGURE 13 HERE

INSERT FIGURE 14 HERE

INSERT FIGURE 15 HERE

8 STIFFNESS PROPERTIES

8.1 INITIAL STIFFNESS

Measurements of shear wave velocities in the new field investigations were taken through a down-hole (DH) test in borehole B1, to a depth of 28 m (Pedro, 2013). The results of the shear wave velocity, V_S, and of the interpreted maximum shear modulus, G_0, profile are shown in Figure 16, together with the results of similar tests compiled by Guedes de Melo (2011) from various sites in Lisbon. Unfortunately, the latter does not distinguish different formations and the data are only used here for reference. However, the new (DH) profile of both V_S and G_0 present a trend similar to that from previous data, generally increasing with depth, and with a concentration of higher values around the depth of the Limestone layer (grey area in Figure 16).

Shear wave velocities measured in the laboratory using bender elements (BE) on triaxial samples (3 tests in the *AE* formation, 2 in the *AP* formation and 1 in the limestone layer) are also presented on Figure 16. In order to define the arrival time of the vertically propagating and horizontally oscillating shear wave between the top and the bottom BE, the ‘first arrival’ method from the time-domain framework was applied (Viggiani & Atkinson, 1995). The BE profile of G_0 in Figure 16 has a trend similar to that from the in-situ DH test, but is significantly smaller in magnitude, although the values are consistent with results published in the literature for similar materials (Hight et al., 2007; Clayton, 2011). Discrepancies like this, between in-situ and laboratory results, have been reported by several authors for other soils (Kokusho, 1987; Ishihara, 1996; Ng & Wang, 2001) and are usually attributed to a combination of factors that were also observed in this study. Despite careful preparation, the set-up and data interpretation of both BE and DH tests involve some uncertainties, which are amplified by scale effect (field vs sample) and greater heterogeneity within the soil mass. However, the most significant factor contributing to this discrepancy is a loss of cementation during sampling of the AE formation. Despite this, the ratio between measured laboratory and field shear moduli is still within the experimentally derived upper and lower boundaries for sands, as proposed by Kokusho (1987), with the average ratio being approximately 25%.

INSERT FIGURE 16 HERE

8.2 STIFFNESS DEGRADATION CURVE

From laboratory experiments

The small-strain stiffness behaviour of the *AE* soil was assessed from the results of 6 isotropically consolidated drained triaxial tests sheared in compression and in extension with a constant p’, at three different mean effective stress levels. The results are shown in Figure 17 as tangent shear stiffness, $G_{tan}(=\Delta({\sigma'}_a-{\sigma'}_r)/(3\Delta\varepsilon_s))$, versus deviatoric strain, $\varepsilon_s(=(2/3)(\varepsilon_a-\varepsilon_r))$. Although the local axial strain instrumentation, comprising two LVDTs on the opposite sides of the sample, could resolve only to about 0.005% strain, the results show the usual trend of modulus decay with increasing deviatoric strains and the G_{tan} values being higher at higher p’. However, for the same stress level (i.e. p’) the differences between the shear degradation curves in compression and in extension are small. The G_0 values from bender element tests, which correspond to very small strains, are superimposed in the figure, where plateaus for the initial part of the stiffness degradation curves would be expected for the three stress levels.

For the *AP* soil 3 drained triaxial compression tests were performed on samples collected at 36.3 m (T-AP-DPC-I-480) and at 39 m (T-AP-DPC-K-480 and T-AP-DPC-I-480*) depth. Two samples, one at each depth, were consolidated isotropically and the third sample anisotropically, with a K_0 equal to 0.7. In all cases a mean effective stress of 480 kPa was applied at the beginning of shearing as explained earlier. The interpreted stiffness curves in Figure 18 show some scatter and, as for the *AE* samples, the smallest recorded deviatoric strains were, on average, above 0.005 %. The initial shear modulus from the BE test indicates a possible plateau of stiffness degradation curves.

Figure 21 displays a summary of normalised (by the current p') stiffness degradation envelopes from all triaxial tests, including the results of the unload-reload loops from five tests on both soils. Although the *AE* soil has generally higher stiffness (AE – Triax) compared to the *AP* soil (AP – Triax), the two ranges overlap. The ranges of normalised G_0 measurements from BE tests on samples from both soils (AE – BE and AP – BE) are marked at very small strains and also show very similar magnitudes of maximum stiffness.

INSERT FIGURE 17 HERE

INSERT FIGURE 18 HERE

From in-situ experiments

The stiffness degradation curves are further interpreted from the unload - reload cycles of the SBPTs and this was done using the idealised theory of expanding cavities (Palmer, 1972). A closed-form solution was proposed by Bolton & Whittle (1999) and Whittle (1999), assuming that the non-linear elastic response of soils can be described by a power law (Equation 3), where α and β are fitting parameters that can be obtained by applying the least squares method to the horizontal stress (σ_h) –

cavity strain (ε_c) curves measured during the SBPT. The tangent shear modulus is then calculated using Equation 4.

$$\sigma_h = \alpha \cdot \varepsilon_c^{\beta} \tag{3}$$

$$G_{tan} = \alpha \cdot \beta \cdot {\varepsilon_c}^{\beta-1} \tag{4}$$

The procedure can be applied both to unload and reload paths of the SBPT cycle, but is often applied only to the latter, as it is thought that the unloading path presents initially some creep, probably related to strain rate effects, making it difficult to select the correct origin of the cycle (Whittle et al., 1993). Figure 19 shows an example of an unload-reload SBPT loop and a fitted power law curve to the reload path of the loop. The authors applied this procedure to 34 reload cycles of the SBPTs carried out by LNEC (1996a, b, c, d) in both soils (11 in the *AP* and 23 in the *AE*). The fitting of all data resulted in the power law parameters $\alpha = 18.367$ and $\beta = 0.643$ (Figure 19). Using Equation 4, the resulting tangent shear modulus normalised by the mean effective stress (estimated assuming that the vertical stress did not change and that the horizontal stress was given by the SBPT) is plotted against the deviatoric strain ($\varepsilon_s = 2/\sqrt{3}\varepsilon_c$) in Figure 20 for the *AE* formation. This range of stiffness degradation curves (AE-SBPT) is added to the overall stiffness plot in Figure 21. A similar procedure was applied to SBPTs performed in the *AP* soil, with the results (AP-SBPT) in Figure 21 indicating a similar range of shear modulus decay to that of the AE-SBPT interpretation. Finally, the normalised G_0 data from the DH test are also added in Figure 21.

Analysis of Figure 21 indicates two important aspects of shear stiffness interpretation for both soils: (i) significant difference, up to 40%, between the in-situ- and laboratory-derived shear modulus, in particular in the nonlinear range (shear strains less than 0.01%); and (ii) overlaps of stiffness envelopes between the two soils at all strain levels and for both experimental sources. The reasons for the former may be attributed to various levels of disturbance of intact samples related to loss of cementation during their extraction, although it was not possible to quantify this with any precision. From the latter observation (ii), considering that this interpretation of shear stiffness is in terms of an overall isotropic stiffness, it is difficult to make a meaningful distinction between the two formations. As a consequence, it seems reasonable to assume the same normalised shear stiffness for both soils and the solid and dashed lines in Figure 21 represent average curves derived from the in-situ and laboratory data respectively. The implication of this interpretation is that any modelling of small-strain stiffness would need to combine the field and laboratory data (e.g. Tatsuoka & Shibuya (1991)). The former is likely to apply for the elastic plateau and in the small-strain range to 0.01% strain, and the latter in the medium to large strain range beyond 0.01% strain where the loss of cementation becomes evident. However, the adopted stiffness degradation curve would need to be validated on a boundary value problem with measured ground movements.

INSERT FIGURE 19 HERE

INSERT FIGURE 20 HERE

INSERT FIGURE 21 HERE

8.3 BULK STIFFNESS

Data relating to the decay of tangent bulk modulus with volumetric strain have been obtained from the isotropic compression tests performed on both soils (Figure 6). In order to determine the tangent bulk modulus, K_{tan} $(= \Delta p'/\Delta\varepsilon_v)$, data from the first loading (L), final unloading (F) and from the unload (U) – reload (R) loops was analysed separately. The bulk modulus curves, normalised by the mean effective stress, p', are plotted against volumetric strain in Figure 22. The results show that for both soils the highest stiffness is mobilised along loading paths, followed by a steep decay. In contrast, along the unloading paths an almost constant bulk modulus was obtained. This path-dependence is more clearly evident in the *AP* formation. For volumetric strains higher than 0.5 %, the majority of the curves have reached a minimum plateau and consequently no major variation of the normalised bulk modulus is expected beyond this strain. If an elastic relationship between G_{tan} and K_{tan} is assumed at small strains ($\varepsilon_s = 0.0001\%\ and\ \varepsilon_v = 0.001\%$) a Poisson's ratio of about 0.17 is estimated.

INSERT FIGURE 22 HERE

9 CONCLUSIONS

The objective of this paper is to contribute new knowledge on the mechanical behaviour of two of the main soil formations in the Lisbon ground stratigraphy, known as the AE and AP formations, based on the results from a new site investigation for the enhanced analysis of the proposed Ivens shaft excavation in Lisbon, Portugal. The investigation comprised both field and laboratory experiments with particular emphasis on the latter. Despite the scatter in experimental evidence observed in both formations caused by the inherent variability of these materials, the interpretation of compressibility and drained strength, has provided a better definition of the layers in the ground profile and a better understanding of their behaviour. It is demonstrated that the more granular AE formation, despite differing degrees of cementation, can be considered as a single unit, apart from the Limestone layer. However, the clayey-silty AP formation needs to be split in two layers, with the top 2 m being of lower strength.

In interpreting stiffness, both of the two formations exhibit similar behaviour with a tangent shear modulus degradation at all strain levels and from both the field and laboratory data. However, significant differences, of up to 40% for very small strains (less than 0.0001%), were observed between the field and laboratory-interpreted shear stiffness. Similar differences, have been observed with the behaviour of other stiff clays and are mainly attributed to loss of cementation during sampling, variability and scale effects and require critical judgement when deriving parameters for numerical modelling. A possible methodology would be to establish a stiffness degradation curve based on the combination of the two sets of results, with the field data used to define the small strain range (less than 0.01% strain) and the data from the laboratory used in the range of medium to large strains.

The results from this investigation, complemented with information from other sites in the Lisbon area, provide a valuable set of data for the selection of an appropriate numerical framework for modelling the general behaviour of these Miocene formations of Lisbon. The data enable calibrations to be made of advanced constitutive models that combine both failure and small-strain soil behaviour.

However, as the results of the current investigation have shown, there is significant variability across the area from the various geological processes, and so consistency of local site conditions with those presented here should be checked.

ACKNOWLEDGEMENTS

The authors wish to acknowledge the support provided by FCT - Fundação para a Ciência e Tecnologia, Portugal (grant reference SFRH / BD / 43845 / 2008) and the Lisbon Metro, for the PhD research of the first author, conducted at Imperial College London, UK and the University of Coimbra, Portugal.

NOTATION

α, β	Fitting parameters
$\Delta \mathrm{u}$	Excess pore water pressure
ε_a	Axial strain
ε_c	Cavity strain
ε_r	Radial strain
ε_s	Shear strain
ε_V	Volumetric strain
κ	Isotropic swelling index
λ	Isotropic compression index
σ'_a	Axial effective stress
σ_h	Horizontal stress
σ'_r	Radial effective stress
σ'_{r0}	Initial radial effective stress
σ'_v	Vertical effective stress
σ'_{v0}	Initial vertical effective stress
ϕ'	Angle of shear resistance
c'	Cohesion
C_C^*	Intrinsic compression index
e_{100}^*	Void ratio in the ICL for a vertical effective stress of 100 kPa
e_L	Void ratio at liquid limit
G_0	Initial shear modulus
G_{tan}	Tangent shear modulus
K_0	Earth pressure coefficient at rest
K_{tan}	Tangent bulk modulus
LL	Liquid limit
p'	Mean effective stress
PL	Plastic limit
q	Deviatoric stress
u_0	Initial pore water pressure
V_S	Shear wave velocity

REFERENCES

Addenbrooke, T. I., Potts, D. M. & Puzrin, A. M. (1997) The influence of pre-failure soil stiffness on the numerical analysis of tunnel construction. *Géotechnique*, **47** (3), pp. 693-712.

Alves, C. A. M., Rodrigues, B., Serralheiro, A. & Faria, A. P. (1980) *The Basaltic deposit of Lisbon*. Reports of the Geological Services of Portugal. pp. 111-134 (in Portuguese).

Antunes, M. T. (1979) *Introduction à la géologie générale du Portugal*. Reports of the Geological Services of Portugal. pp. 72-85 (in French).

Antunes, M. T., Legoinha, P., Cunha, P. P. & Pais, J. (2000) High resolution stratigraphy and miocene facies correlation in Lisbon and Setubal Peninsula (Lower Tagus basin, Portugal). In *Proceedings of the 1st Congress about the Cenozoic era in Portugal, Lisbon*. pp. 183-190.

ASTM (2006), D 2487, *Standard practice - Classification of soils for engineering purposes (unified soil classification system)*. USA, American Society for Testing and Materials.

Atkinson, J. H. (1993) *An Introduction to the Mechanics of Soils and Foundations through critical state soil mechanics.* McGraw-Hill Book Company (UK) Ltd. pp. 356.

Bolton, M. D. & Whittle, R. W. (1999) A non-linear elastic perfectly plastic analysis for plane strain undrained expansion tests. *Géotechnique*, **49** (1), pp. 133-141.

Burland, J. B. (1990) On the compressibility and shear-strength of natural clays. *Géotechnique*, **40** (3), pp. 329-378.

Cenorgeo (2008) *Design project of Ivens Shaft - Baixa-Chiado metro station of the Lisbon Metro*. Cenorgeo. pp. 350 (in Portuguese).

Clayton, C. R. I. (2011) Stiffness at small strain: research and practice. *Géotechnique*, **61** (1), pp. 5-37.

Cotecchia, F. & Chandler, R. J. (2000) A general framework for the mechanical behaviour of clays. *Géotechnique*, **50** (4), pp. 431-447.

Cotter, J. C. B. (1956) *The marine Miocene of Lisbon*. Reports of the Geological Services of Portugal. pp. 9-87 (in Portuguese).

Dias, J. M. A., Rodrigues, A. & Magalhães, F. (1997) *Evolution of the coast line in Portugal since the Last Glacial Maximum*. Works of Quaternary. pp. 53-66 (in Portuguese).

Dias, R. & Pais, J. (2009) Homogenisation of the Cenozoic geological mapping of the Lisbon Metropolitan Area (AML). *Geological Publications*, **96** pp. 39-50. (in Portuguese).

Franzius, J. N., Potts, D. M. & Burland, J. B. (2005) The influence of soil anisotropy and K-0 on ground surface movements resulting from tunnel excavation. *Géotechnique*, **55** (3), pp. 189-199.

Guedes de Melo, P. (2008) Characterization of "Areolas da Estefânia" formation from the numerical modelling of the pressuremeter test. *Geotecnia*, **113** pp. 5-21. (in Portuguese).

Guedes de Melo, P. (2011) *Wave velocities in the Miocene formations of Lisbon*. Personal Communication. (in Portuguese).

Hight, D. W., Gasparre, A., Nishimura, S., Minh, N. A., Jardine, R. J. & Coop, M. R. (2007) Characteristics of the London Clay from the Terminal 5 site at Heathrow Airport. *Géotechnique*, **57** (1), pp. 3-18.

Ishihara, K. (1996) *Soil Behaviour in Earthquake Geotechnics.* Oxford Science Publications. pp. 385.

Kokusho, T. (1987) In situ dynamic soil properties and their evaluation. In *Proceedings of the 8th Asian Regional Conference on Soil Mechanics and Foundation Engineering, Kyoto, Japan*. Vol. 2, pp. 215-435.

LNEC (1996a) *Pressuremeter tests in Baixa-Chiado station - Lisbon subway*. LNEC. pp. 97 (in Portuguese).

LNEC (1996b) *Pressuremeter tests in Alameda station - Lisbon subway*. LNEC. pp. 98 (in Portuguese).

LNEC (1996c) *Pressuremeter tests in Alameda station - Lisbon subway*. LNEC. pp. 140 (in Portuguese).

LNEC (1996d) *Pressuremeter tests in Baixa-Chiado station - Lisbon subway*. LNEC. pp. 141 (in Portuguese).

Ludovico Marques, M. A. & Sousa Coutinho, A. G. F. (2004) Cambridge selfboring pressuremeter and Ménard pressuremeter: contribution to a mechanical characterisation of Miocene soils of Lisbon and Loures. In *Proceedings of the IX - National Conference in Geotechnics, Aveiro*. Vol. I, pp. 299-308 (in Portuguese).

Lunne, T., Berre, T. & Strandvik, S. (1997) Sample disturbance effects in soft low plastic Norwegian clay. In *Proceedings of the Symposium on recent developments in soil and pavement mechanics*.

Marques, F. E. R. (1998) *Analysis of the observed behaviour of a tunnel open in the Miocenic formations of Lisbon*. Master's thesis. University of Coimbra, Coimbra (in Portuguese).

Moitinho de Almeida, I. (1991) *Geotechnical characteristics of the Lisbon soils*. PhD thesis. University of Lisbon, Lisbon (in Portuguese).

Ng, C. W. W. & Wang, Y. (2001) Field and laboratory measurements of small strain stiffness of decomposed granites. *Soils and Foundations*, **41** (3), pp. 57-71.

Palmer, A. C. (1972) Undrained plane-strain expansion of a cylindrical cavity in clay - simple interpretation of pressuremeter test. *Géotechnique*, **22** (3), pp. 451-457.

Pedro, A. (2013) *Geotechnical investigation of Ivens shaft in Lisbon*. PhD Thesis. Imperial College London, London, UK.

Postiglione, P., Abrantes, J. R. d. C., Pinto, F. A. D., Mosiici, P. & Altan, V. D. (1997) Consolidations by jet grouting previous to escavations of the western station of the "Baixa-Chiado" twin stations of the Lisbon Metro. In *Proceedings of the VI National Conference in Geotechnics, Lisbon*. pp. 1125-1134 (in Portuguese).

Skempton, A. W. (1953) The Colloidal "Activity" of Clays. In *Proceedings of the Third International Conference on Soil Mechanics and Foundation Engineering, Switzerland*. pp. 57-61.

Tatsuoka, F. & Shibuya, S. (1991) Deformation characteristics of soils and rocks from field and laboratory tests. In *Proceedings of the 9th Asian Regional Conference on Soil Mechanics and Foundation Engineering, Bangkok*. Vol. 2, pp. 101-170.

Taylor, D. W. (1948) *Fundamentals of soil mechnics.* John Wiley & Sons, Inc. pp. 711.

Viggiani, G. & Atkinson, J. (1995) Interpretation of bender element tests. *Géotechnique*, **45** (1), pp. 149-154.

Whittle, R. W., Dalton, J. C. P. & Hawkins, P. G. (1993) Shear modulus and strain excursion in the pressuremeter test. In *Proceedings of the Predictive Soil Mechanics*, pp. 768-782.

Whittle, R. W. (1999) Using non-linear elasticity to obtain the engineering properties of clay - a new solution for the self boring pressuremeter test. *Ground Engineering*, **32** (5), pp. 30-34.

Zdravkovic, L., Potts, D. M. & John, H. D. S. (2005) Modelling of a 3D excavation in finite element analysis. *Géotechnique*, **55** (7), pp. 497-513.

FIGURE CAPTIONS

Figure 1 – Location of the Baixa-Chiado station and Ivens shaft in Lisbon downtown (modified from Google Earth)

Figure 2 – Ivens shaft soil profile

Figure 3 – Particle size distribution and index properties of the Ivens shaft site ground profile (Pedro, 2013)

Figure 4 – Scheme of the total stress paths adopted in the triaxial tests

Figure 5 – K_0 profile obtained with SBPTs (Pedro, 2013)

Figure 6 – Isotropic compression curves of the *AE* and *AP* soils

Figure 7 – Oedometer tests performed on the AP soil

Figure 8 – Stress ratio – axial strain curves from all triaxial tests on the AE soil

Figure 9 – Volumetric strains from drained triaxial tests on the AE soil

Figure 10 – Excess pore pressures from undrained triaxial tests on the AE soil

Figure 11 – Effective stress-paths from all triaxial tests on the AE soil

Figure 12 – Stress ratio – axial strain curves from all triaxial tests on the AP soil

Figure 13 – Volumetric strains from drained triaxial tests on the AP soil

Figure 14 – Excess pore pressures from drained triaxial tests on the AP soil

Figure 15 – Effective stress-paths from all triaxial tests on the AP soil

Figure 16 – Results of seismic tests at the Ivens shaft location

Figure 17 – Stiffness degradation curves for the AE soil

Figure 18 – Stiffness degradation curves for the AP soil

Figure 19 – An example of an unload-reload SBPT loop employed in the derivation of shear stiffness degradation curves

Figure 20 – Normalised shear stiffness degradation curves for the AE soil derived from the reload paths of SBPT loops

Figure 21 – Comparison of the normalised tangent shear modulus curves from field and laboratory tests on AE and AP soils

Figure 22 – Normalised bulk modulus degradation curves for AE and AP soils

APPENDIX

Table 1– Tests performed on intact samples retrieved from the boreholes drilled in the backyard of the Quintão building (Pedro, 2013)

Type of test	Lithology	Number of tests	Sample dimensions	Designation code	Depth (m)	σ'_{vo} (kPa)	σ'_{ro} (kPa)	u_0 (kPa)	Drainage
Oedometer **(O)**	AP	3	50x19 (mm)	OED36.5	36.5	-	-	-	-
				OED37.5	37.5	-	-	-	-
				OED40.0	40.0	-	-	-	-
Isotropic compression **(I)**	AE	3	38x76 (mm)	I-AE-08.5	8.5	50	50	350	Drained
				I-AE-18.0	18.0	50	50	200	Drained
				I-AE-21.5	21.5	50	50	300	Drained
	AP	1	38x76 (mm)	I-AP-39.5	39.5	50	50	150	Drained
Bender Element **(BE)**	AE	3	38x76 (mm)	BE-AE-07.7	7.7	50	50	300	Drained
				BE-AE-18.3	18.3	50	50	300	Drained
				BE-AE-21.5	21.5	50	50	300	Drained
	LI	1	38x76 (mm)	BE-LI-12.5	12.5	200	200	300	Drained
	AP	2	38x76 (mm)	BE-AP-36.5	36.5	100	70	300	Drained
				BE-AP-36.2	36.2	100	100	300	Drained
Triaxial **(T)**	AE	14	38x76 (mm)	T-AE-DPC-I-130	8.0	130	130	500	Drained
				T-AE-DPC-I-300	18.0	300	300	300	Drained
				T-AE-DPC-I-400	21.0	400	400	300	Drained
				T-AE-DPC-I-300*	4.1	300	300	400	Drained
				T-AE-DPE-I-130	7.8	130	130	400	Drained
				T-AE-DPE-I-300	18.6	300	300	300	Drained
				T-AE-DPE-I-400	21.3	400	400	200	Drained
				T-AE-UCD-I-130	8.6	130	130	500	Undrained
				T-AE-UCD-I-300	18.5	300	300	400	Undrained
				T-AE-UED-I-130	6.2	130	130	500	Undrained
				T-AE-UEI-I-130	8.0	130	130	200	Undrained
				T-AE-UCI-I-130	6.4	130	130	500	Undrained
				T-AE-DCI-I-130	8.2	130	130	300	Drained
				T-AE-DCI-I-300	18.2	300	300	300	Drained
	AP	5	38x76 (mm)	T-AP-DPC-K-480	40.4	600	420	150	Drained
				T-AP-DPC-I-480*	38.7	480	480	300	Drained
				T-AP-DCD-K-480	39.9	600	420	150	Drained
				T-AP-UCD-K-480	38.8	600	420	150	Undrained
				T-AP-UCI-K-480	40.2	600	420	150	Undrained
	TAP	2	38x76 (mm)	T-TAP-DPC-I-480	36.3	480	480	300	Drained
				T-TAP-UCI-K-480	37.7	600	420	150	Undrained

Test designation code (Example):

Lithology: AE - "Areolas da Estefânia"; AP - "Argilas e Calcários dos Prazeres"; TAP – Top of "Argilas e Calcários dos Prazeres"; LI – Limestones

Shearing path: DPC - drained compression with constant p'; DPE - drained extension with constant p'; DCD - drained compression with decrease p'; DCI - drained compression with increase p'; UCD - undrained compression with decrease p'; UED - undrained extension with decrease p'; UEI - undrained extension with increase p'; UCI - undrained compression with increase p';

Consolidation: I - isotropic consolidation; K - anisotropic consolidation (K_0=0.7)

Oedometer: Type of test – Lithology – Sample Depth (***O-AP-36.5***)

Isotropic compression: Type of test – Lithology – Sample Depth (***I-AE-18.0***)

Bender elements: Type of test – Lithology – Sample Depth (***BE-AE-07.7***)

Triaxial: Type of test – Lithology – Shearing path – Consolidation - initial mean stress (***T-AE-DPC-I-130***)

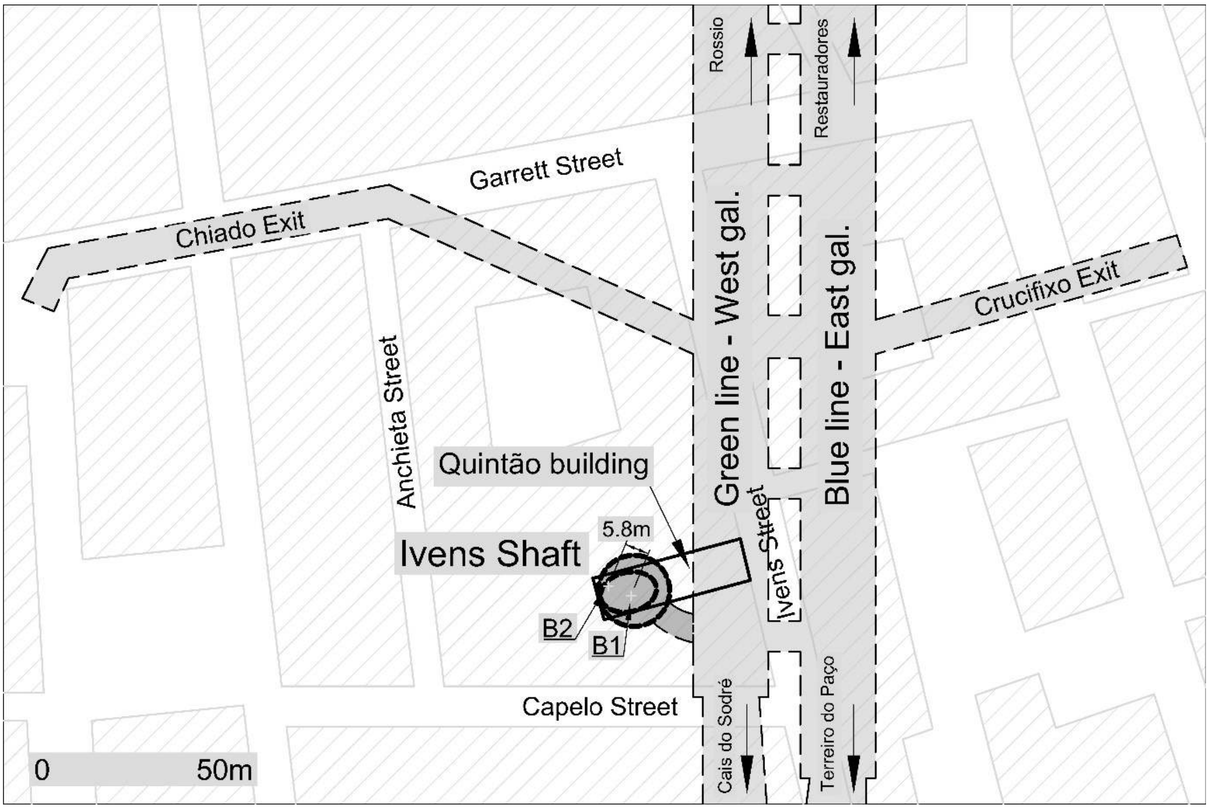

Figure 1 – Location of the Baixa-Chiado station and Ivens shaft in Lisbon downtown

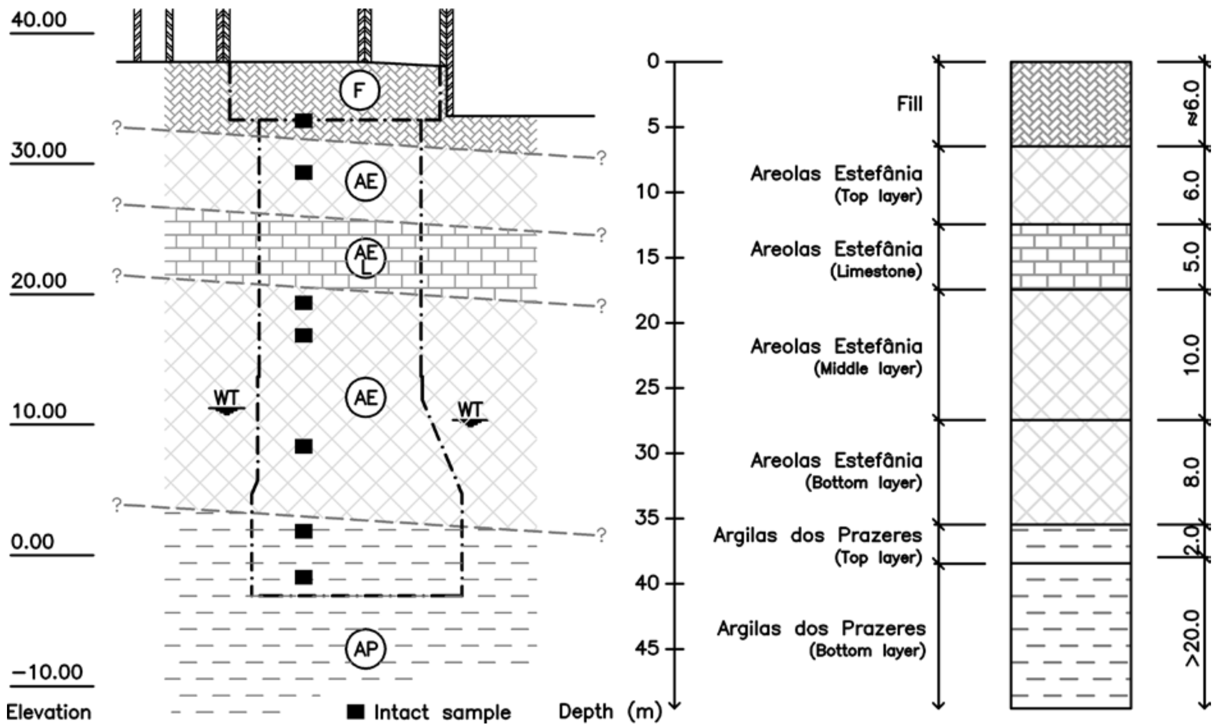

Figure 2 – Ivens shaft soil profile

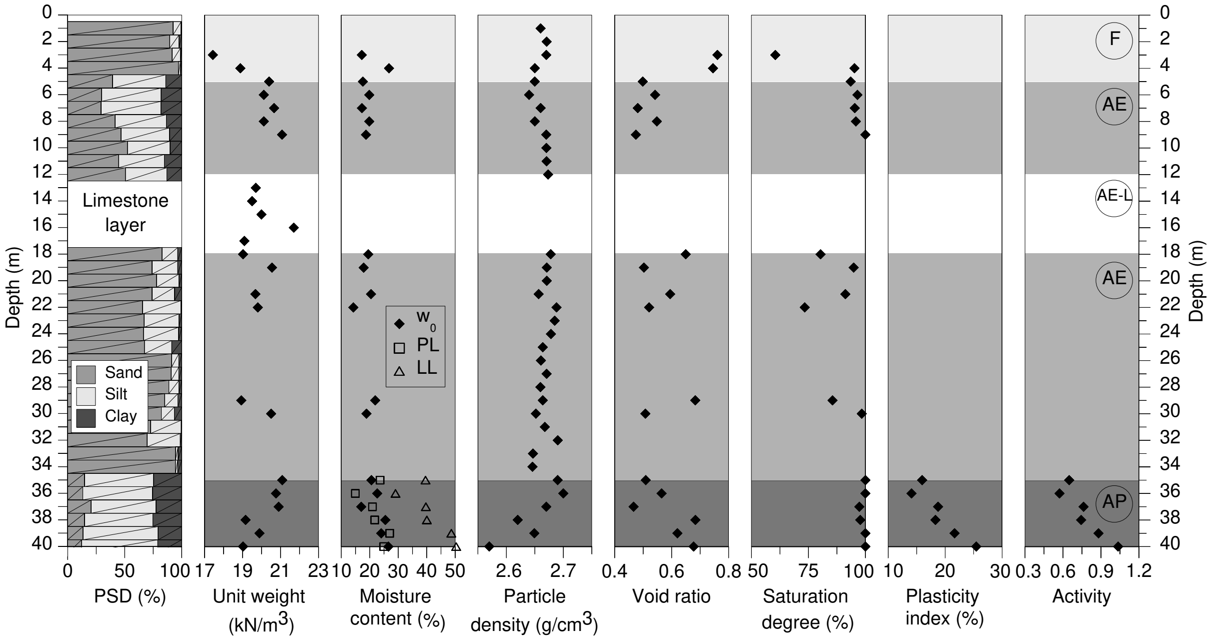

Figure 3 – Particle size distribution and index properties of the Ivens shaft site ground profile (Pedro, 2013)

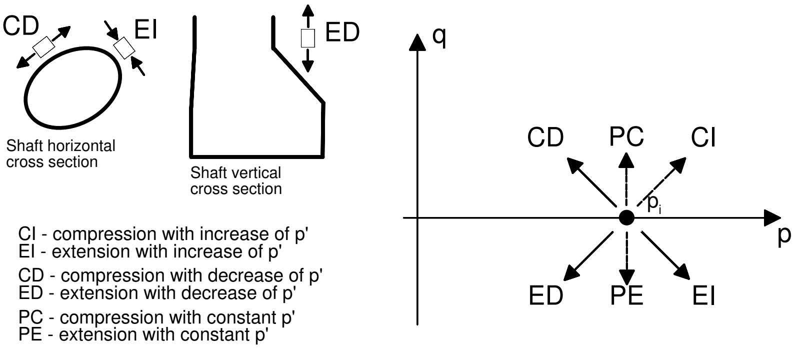

Figure 4 – Scheme of the total stress paths adopted in the triaxial tests

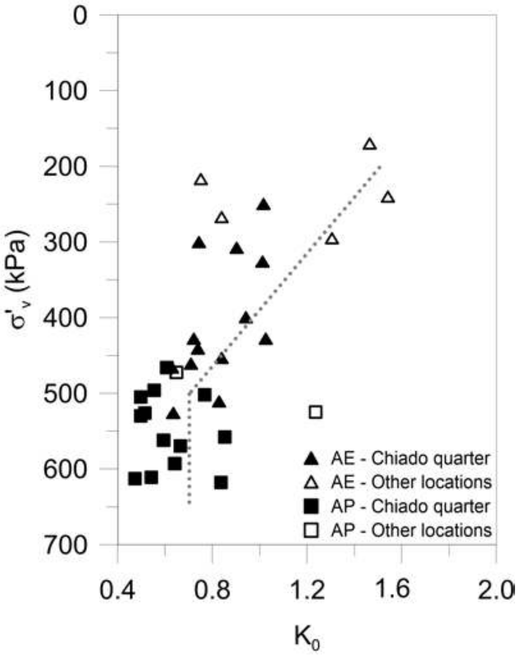

Figure 5 – K_0 profile obtained with SBPTs (Pedro, 2013)

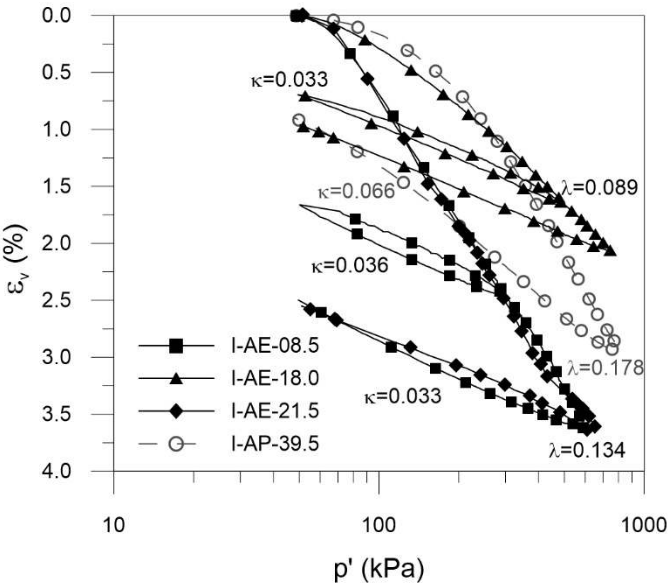

Figure 6 – Isotropic compression curves of the *AE* and *AP* soils

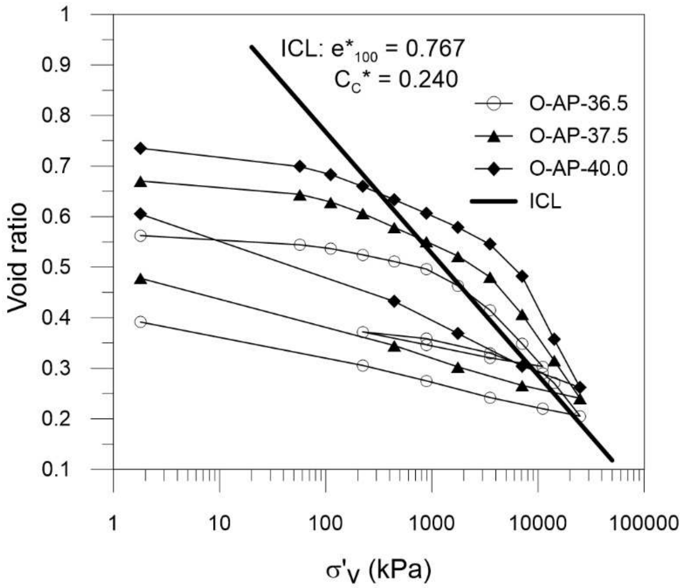

Figure 7 – Oedometer tests performed on the AP soil

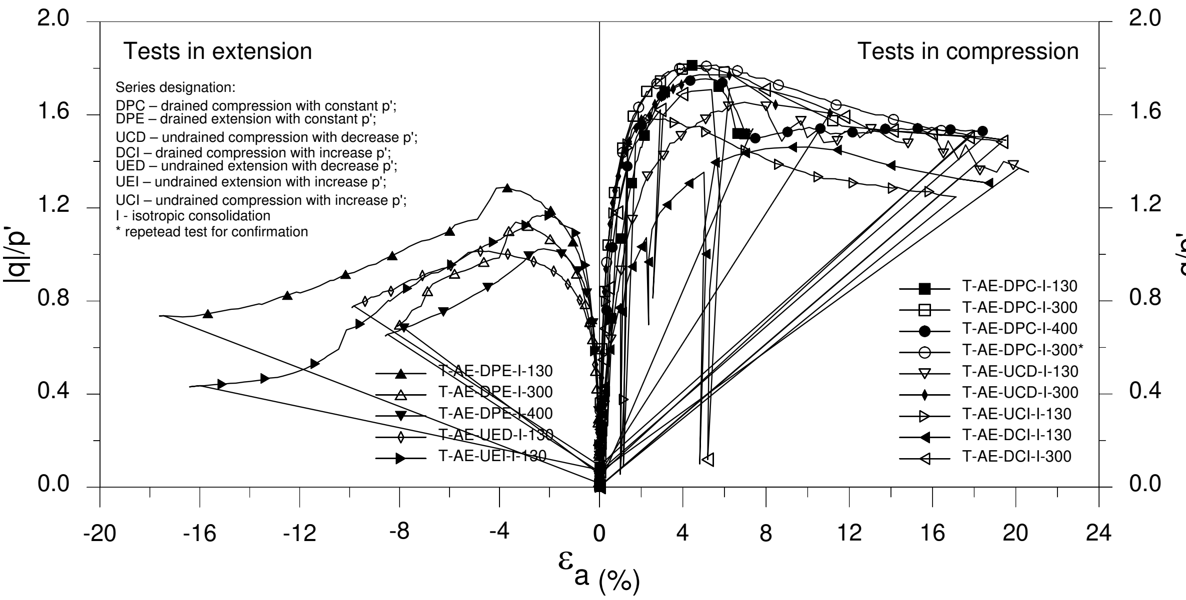

Figure 8 – Stress ratio – axial strain curves from all triaxial tests on the AE soil

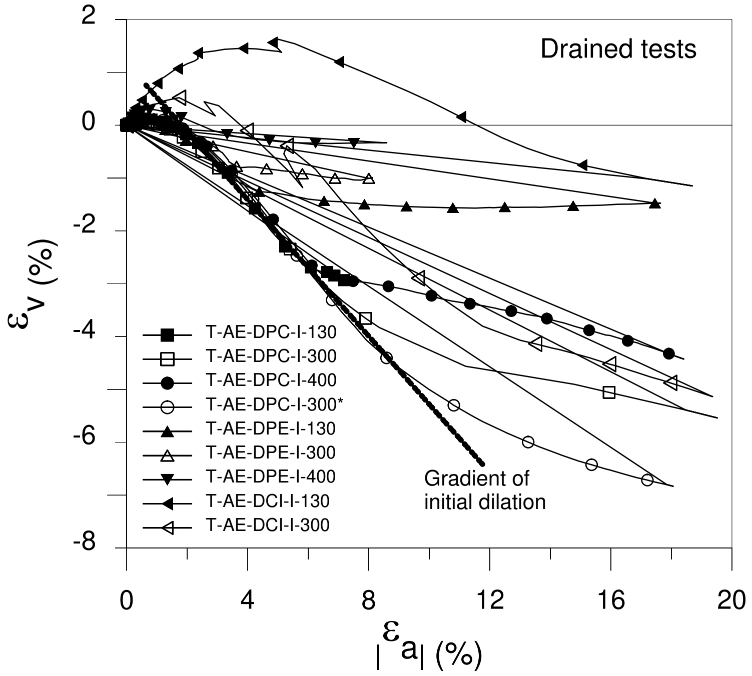

Figure 9 – Volumetric strains from drained triaxial tests on the AE soil

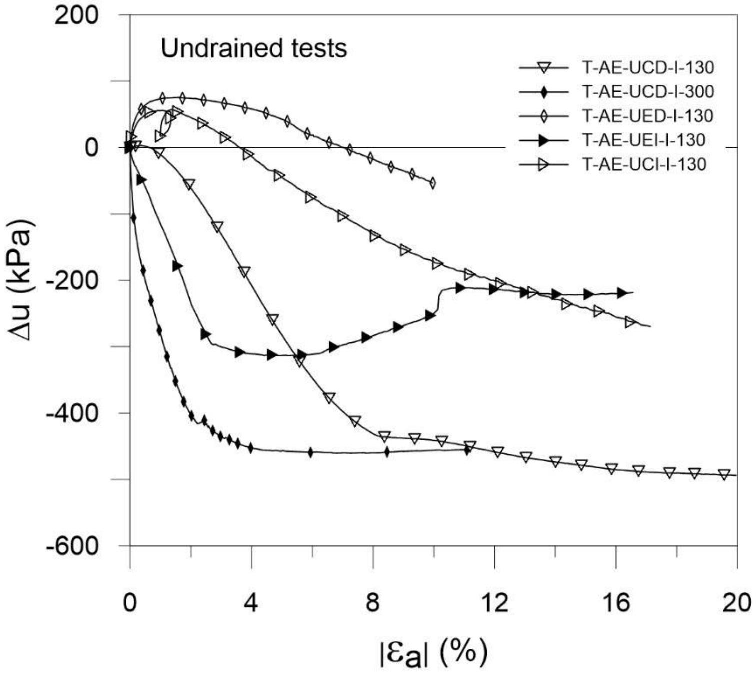

Figure 10 – Excess pore pressures from undrained triaxial tests on the AE soil

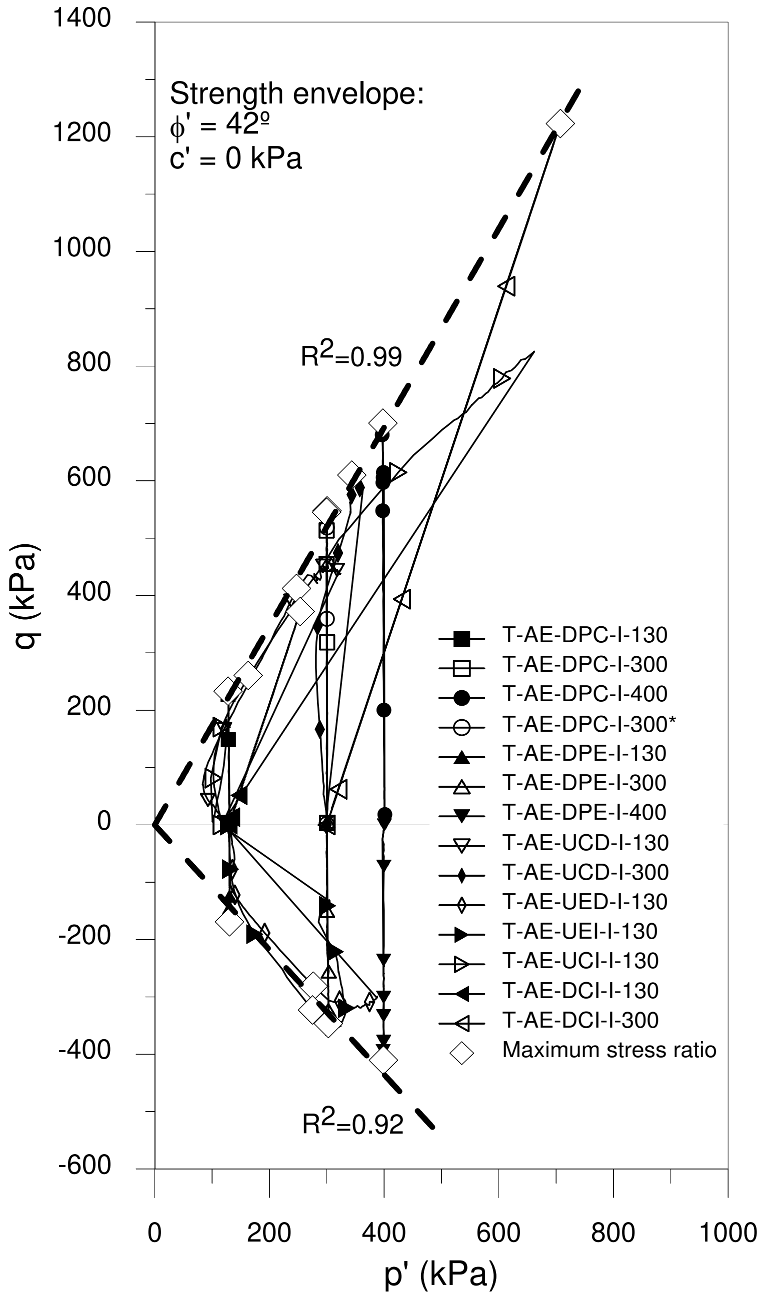

Figure 11 – Effective stress-paths from all triaxial tests on the AE soil

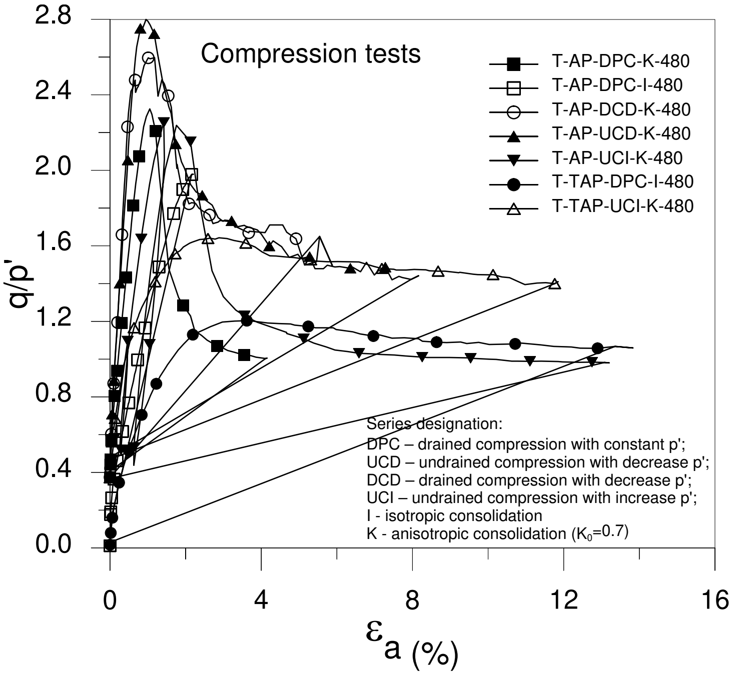

Figure 12 – Stress ratio – axial strain curves from all triaxial tests on the AP soil

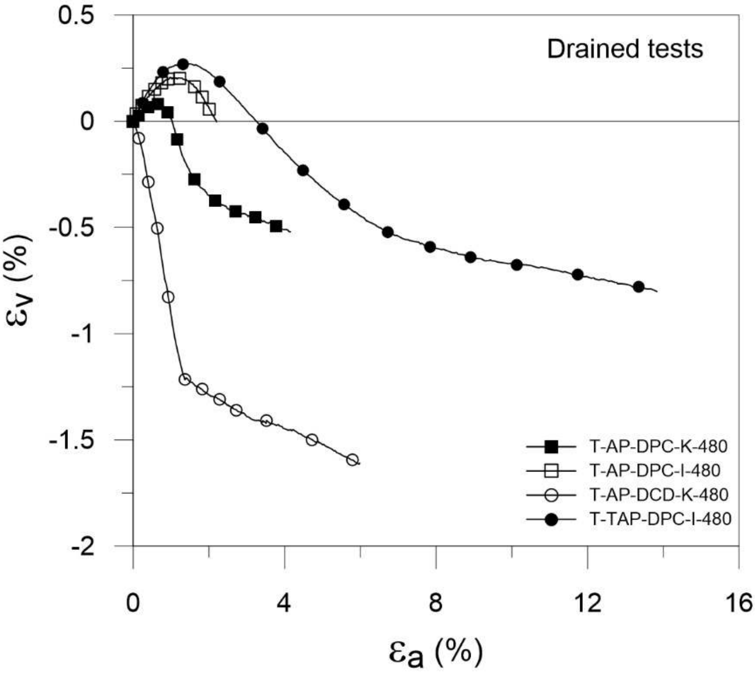

Figure 13 – Volumetric strains from drained triaxial tests on the AP soil

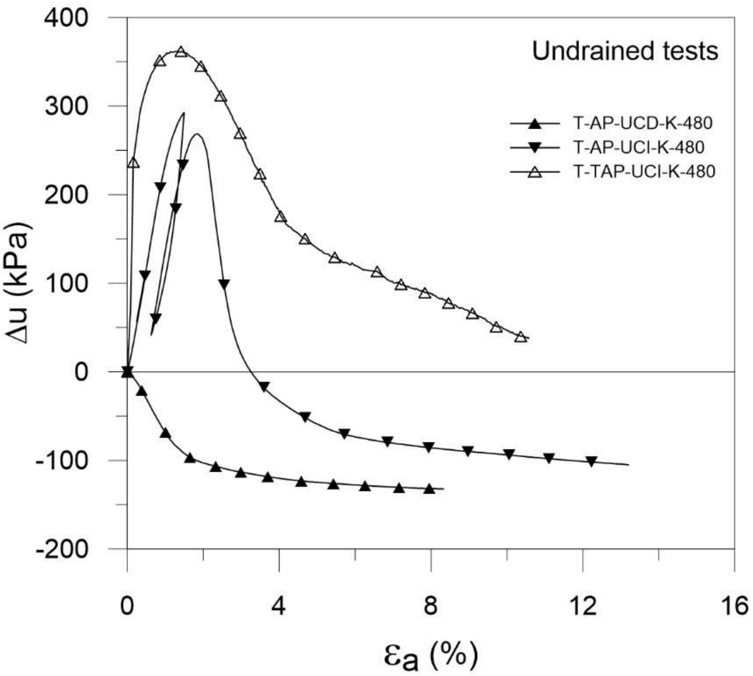

Figure 14 – Excess pore pressures from drained triaxial tests on the AP soil

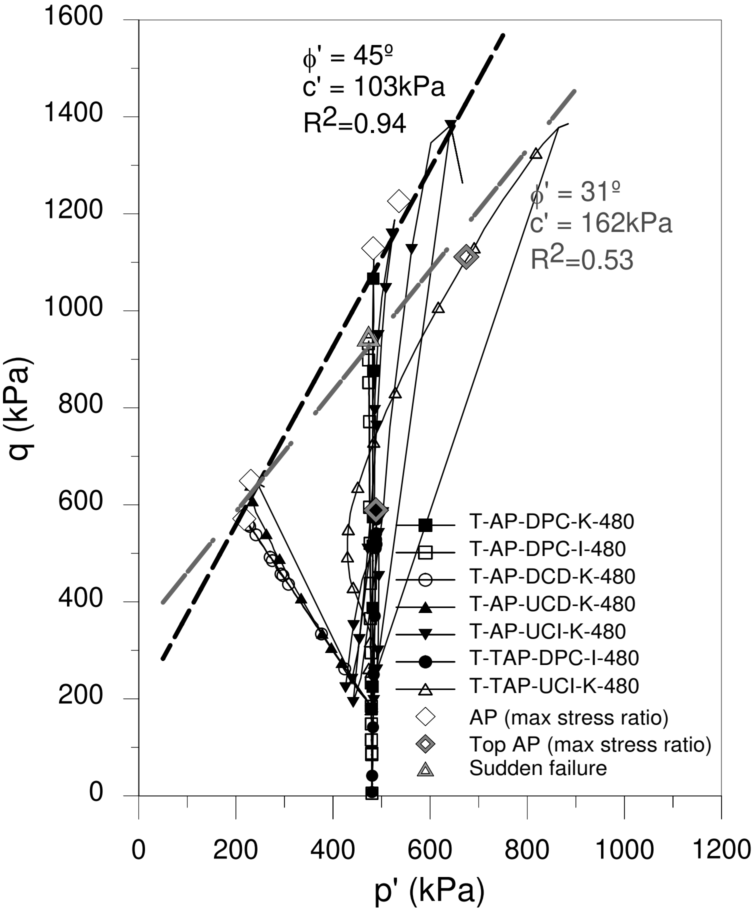

Figure 15 – Effective stress-paths from all triaxial tests on the AP soil

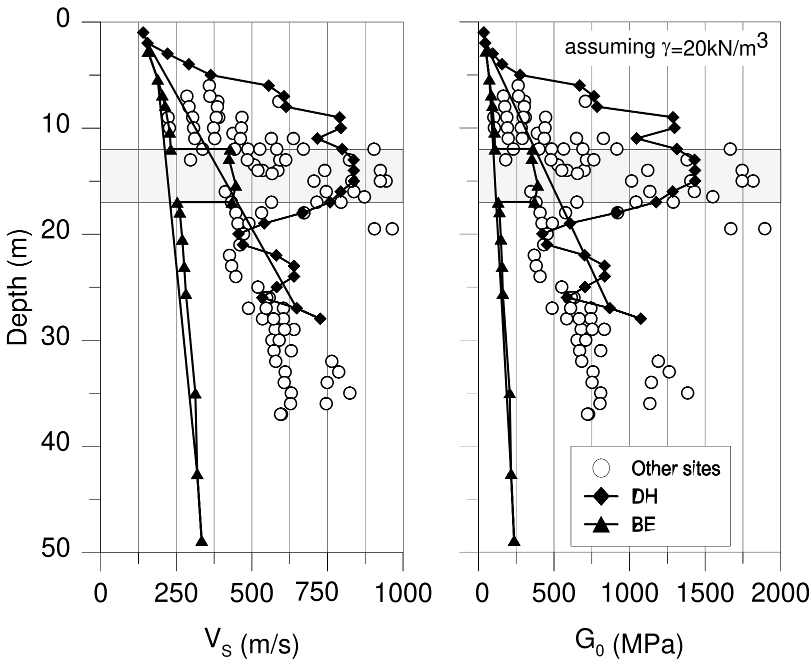

Figure 16 – Results of seismic tests at the Ivens shaft location

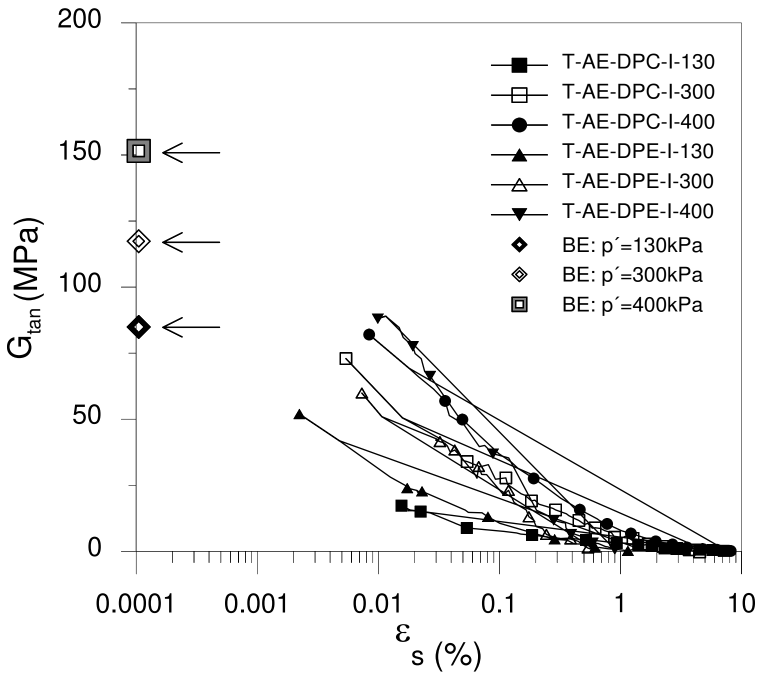

Figure 17 – Stiffness degradation curves for the AE soil

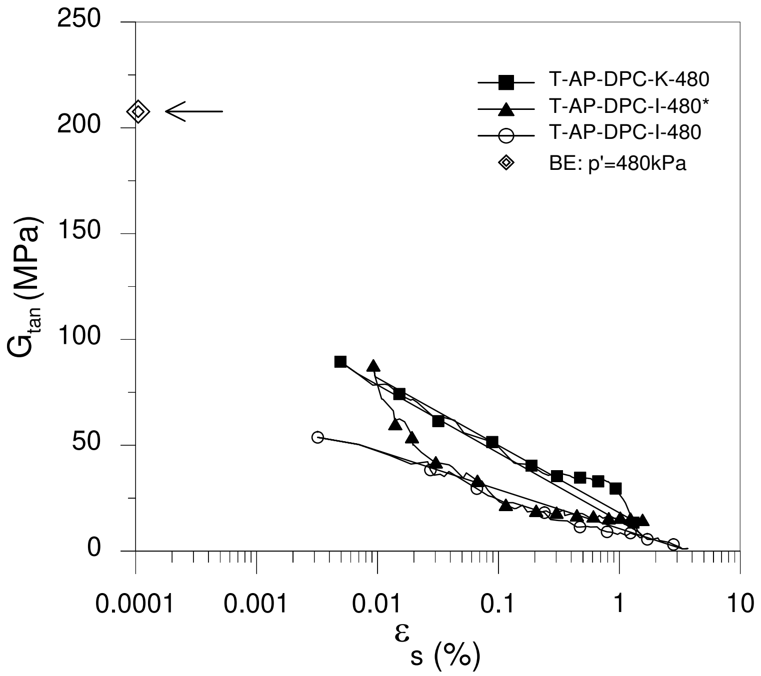

Figure 18 – Stiffness degradation curves for the AP soil

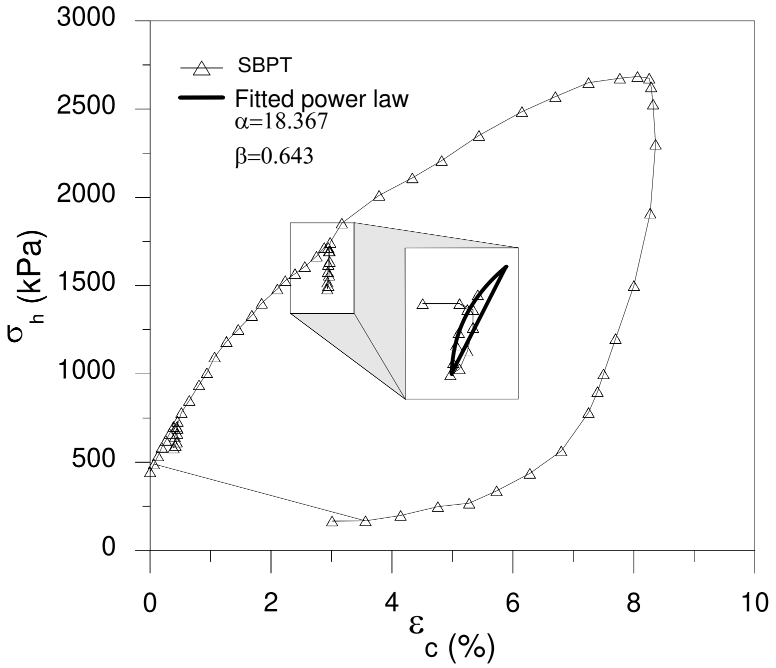

Figure 19 – An example of an unload-reload SBPT loop employed in the derivation of shear stiffness degradation curves

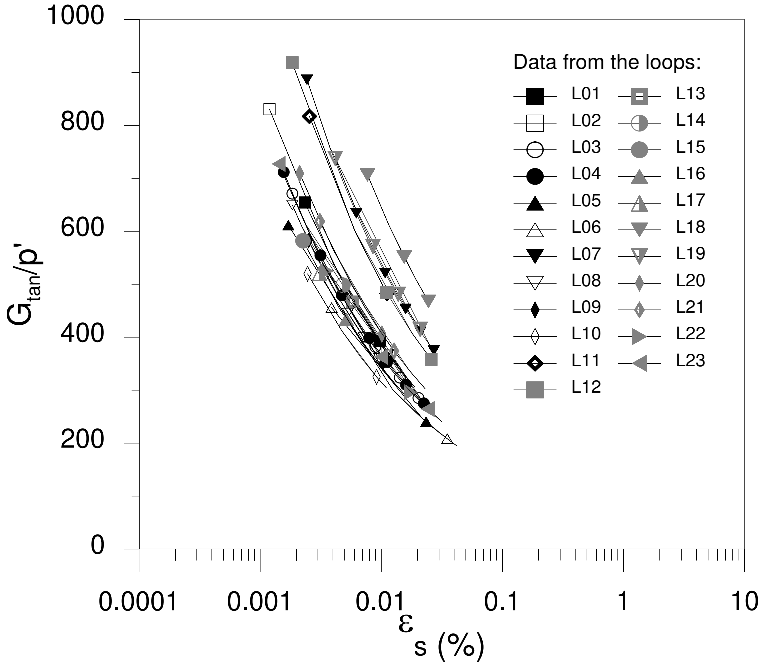

Figure 20 – Normalised shear stiffness degradation curves for the AE soil derived from the reload paths of SBPT loops

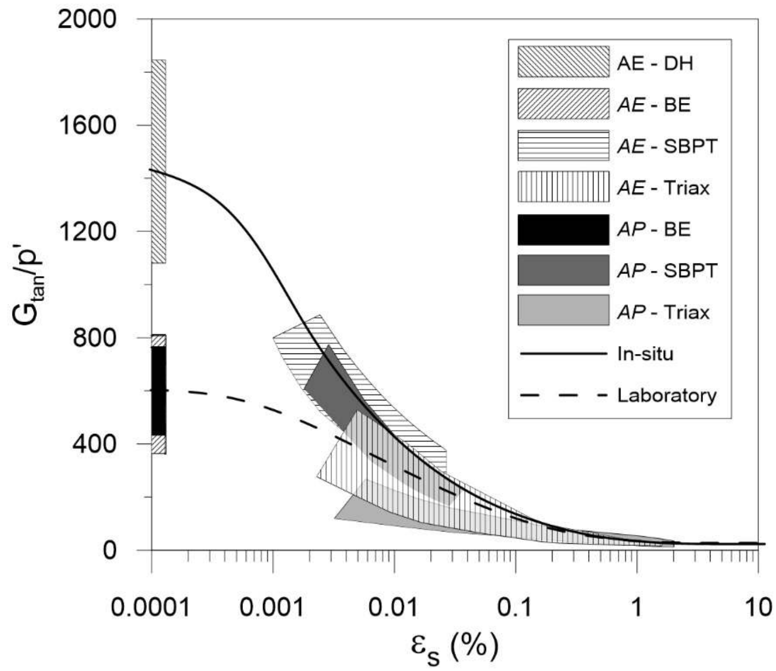

Figure 21 – Comparison of the normalised tangent shear modulus curves from field and laboratory tests on AE and AP soils

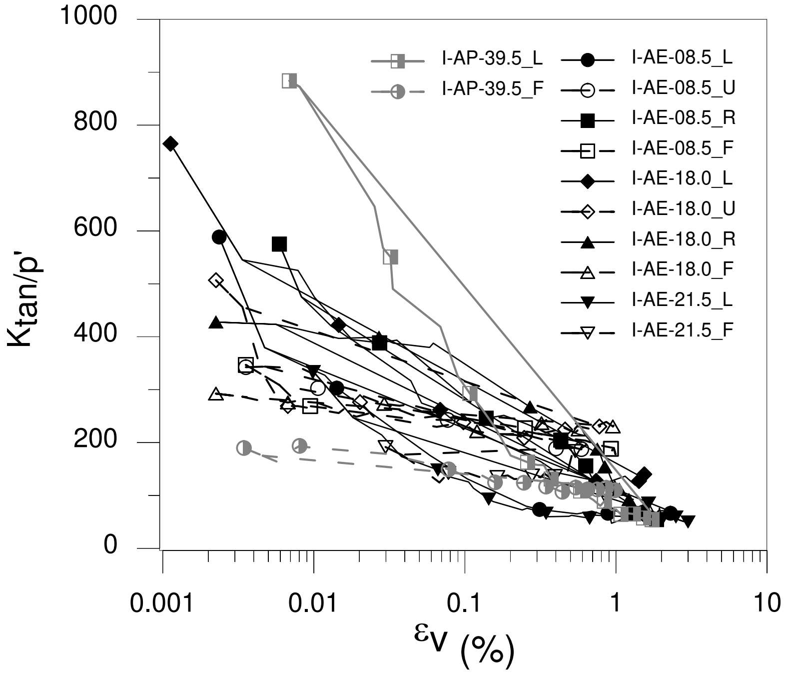

Figure 22 – Normalised bulk modulus degradation curves for AE and AP soils